Report no. changed (Mar 2006): SR-290-UU

SACLANTCEN REPORT
serial no: SR-290

SACLANT UNDERSEA
RESEARCH CENTRE
REPORT

PENETRATION OF ACOUSTIC WAVES INTO SANDY SEAFLOORS AT LOW GRAZING ANGLES: THE HELMHOLTZ-KIRCHHOFF APPROACH

E. Pouliquen, A.P. Lyons, N.G. Pace

August 1998

Report no. changed (Mar 2006): SR-290-UU

SACLANT Undersea Research Centre
Viale San Bartolomeo 400
19138 San Bartolomeo (SP), Italy

tel: +39-0187-540.111
fax: +39-0187-524.600

e-mail: library@saclantc.nato.int

NORTH ATLANTIC TREATY ORGANIZATION

Penetration of acoustic waves into sandy seafloors at low grazing angles: the Helmholtz-Kirchhoff approach

E. Pouliquen, A. P. Lyons, N. G. Pace

The content of this document pertains to work performed under Project 033-2 of the SACLANTCEN Programme of Work. The document has been approved for release by The Director, SACLANTCEN.

Jan L. Spoelstra
Director

intentionally blank page

Report no. changed (Mar 2006): SR-290-UU

Penetration of acoustic waves into sandy seafloors at low grazing angles: the Helmholtz-Kirchhoff approach

E. Pouliquen, A. P. Lyons, N. G. Pace

Executive Summary:

Mines which are completely buried in certain types of ocean sediments are generally considered undetectable by conventional high frequency minehunting sonars. This is due to the very low levels of energy that are transmitted into the sediment for these frequencies at the low grazing angles favored for minehunting operations. As the attenuative effect of the sediment is less at lower frequencies, the possibility of using much lower frequency sonars at low grazing angles in order to enhance the ability to hunt buried mines has been investigated.

The physics of sound penetration into sediment is an area of active research as a good understanding of this phenomenon is essential to the design of systems capable of hunting buried mines. Anomalously high levels of sound penetration into ocean sediments have been reported, and competing hypotheses have been formulated to explain this effect.

This report investigates roughness of the sediment interface as the candidate mechanism by which anomalously high levels of energy are transmitted into the sediment. The conclusion is that roughness of the sediment interface is very likely to be the cause of the anomalous sound penetration at low grazing angles.

Future work in this area will concentrate on evaluating the amount of acoustic energy scattered by a buried mine and on the ability to detect them at current minehunting frequencies as well as at lower frequency where penetration is enhanced.

Report no. changed (Mar 2006): SR-290-UU

intentionally blank page

Penetration of acoustic waves into sandy seafloors at low grazing angles: the Helmholtz-Kirchhoff approach

E. Pouliquen, A. P. Lyons, N. G. Pace

Abstract:

The Helmholtz-Kirchhoff integral is applied to model the penetration of sound waves into sandy seafloors at grazing angles above and below the critical angle. Although the conditions for the validity of the Kirchhoff approximation can be limiting, this approximation should be valid at high frequency for gently undulating seafloor surfaces even at moderate to low grazing angles, providing that the self-shadowing effect is carefully removed. The analytical development of the method is first presented, followed by numerical examples. Simulations and data acquired at sea are in very good agreement in the 2-15 kHz band (Maguer *et al.* [SACLANTCEN Report, SR-287, April 1998]). The model predicts, in agreement with the 2-15 kHz acoustic data, the frequency at which the contributions due to roughness effects begin to dominate those due to the evanescent wave. Secondary effects such as Bragg interference patterns and the loss of signal coherence with grazing angle or depth are correctly predicted. The model simulations strongly suggest that roughness of the sediment interface is most likely the cause of anomalous sound penetration into the seabed.

Résumé:

L'intégrale d'Helmholtz-Kirchhoff est utilisée pour modéliser la pénétration des ondes acoustiques dans un fond de sable à des angles de rasance supérieurs et inférieurs à l'angle critique. Bien que les conditions de validité de l'approximation de Kirchhoff puissent être limitantes, cette approximation est valide à haute fréquence pour des surfaces peu rugueuses, même pour des angles de rasance assez faibles, dans la mesure oú l'effet d'ombre est correctement supprimé. Le développement analytique de la méthode est d'abord présenté et est suivi d'exemples numériques. Les simulations sont en bon accord avec les données acquises en mer (Maguer et al. [SACLANTCEN Report, SR-287, April 1998]). Le modèle prédit, conformément aux données acquises dans la gamme de fréquence de 2 à 15 kHz, la fréquence à laquelle la contribution due à l'effet de rugosité commence à dominer celle due à l'onde évanescente. Des effets secondaires tels que l'apparition de franges d'interférence de Bragg ainsi que la dépendence de la perte de la cohérence du signal avec l'angle de rasance et la profondeur dans le sediment sont aussi correctement prédits. Les simulations du modèle suggèrent fortement que la rugosité d'interface est la cause la plus probable de la pénétration anormale du son dans les fonds marins.

Keywords: seafloor ○ surface scattering ○ sound penetration ○ Kirchhoff ○ evanescent wave ○ time domain

Contents

1

Introduction

Interest in the penetration of acoustic energy into the seafloor below the critical grazing angle has increased with the relatively recent discovery that levels are often above those predicted by elastic wave theory for smooth seabeds (Maguer, *et al.* [1], Chotiros [2] [3], Lopes [4], Osler *et al.* [5]). In these experiments the inclusion of various probable penetration mechanisms such as the evanescent wave or bounded beam effects (Jensen and Schmidt [6], Williams, *et al.* [7]) underestimated the actual level of acoustic energy transmitted across the water-sediment interface. Other mechanisms which may explain these anomalous levels include the Biot slow wave (Chotiros [2]) and roughness scattering (Thorsos *et al.* [8]). Using a broad band parametric system (2-15 kHz) Maguer *et al.* [1], have been able to map, for their experimental conditions, the point in frequency where the dominant mechanisms affecting the pressure field in the sediment changes from the evanescent wave and bounded beam effects to another mechanism, which they attribute to roughness scattering. While the question of which mechanism, interface roughness or Biot slow wave, plays a greater role in the transmission of acoustic energy into the seafloor at subcritical grazing angles has not yet been definitively answered, it is becoming increasingly accepted that roughness is, in many cases, an important contributor (Simpson and Houston [9], Maguer *et al.* [1]). Roughness scattering models of subcritical penetration of sound into marine sediments have generally used perturbation theory with an isotropic power law spectrum to describe seafloor roughness (Thorsos *et al.* [8], Jackson *et al.* [10]). Both the assumption of an isotropic power law spectrum and the validity of perturbation theory come into question for many shallow water sandy seafloors.

In shallow water, the interaction of currents with the wave-sediment interface can be very strong, commonly producing relatively large, oriented, quasi-periodic features, i.e., ripple fields. Ripple fields are usually formed in granular deposits with little or no cohesion between particles and are observed in both steady and oscillatory flows. At low sediment transport rates, the wavelength of the ripples is directly proportional to the orbital amplitude of the fluid outside the boundary layer with a constant of proportionality which does not depend greatly on grain size or density. These types of ripples are often called vortex ripples because of the vortex which forms in the lee of each crest and have waveheight-to-wavelength ratios of $0.1 - 0.25$ (Sleath [11]). Once the ripple field is formed it can remain when the fluid velocity falls below the limit for sediment movement. The ripple field structure will remain until it is changed by another mechanism such as bioturbation or another strong surface wave event. For sandy seafloors in shallow water, these roughness formation mechanisms are such that the isotropic power law is often not an accurate description of the roughness spectrum as it ignores the larger scale anisotropic and near monochromatic structure (2 - 10 cycles/m) that exists.

Information on the exact form of the small scale roughness spectra for shallow water seafloors is usually based on stereo photogrammetric methods (Akal [12], Briggs [13], Wheatcroft [14]) with results often presented in the form of a one-dimensional spectrum. One-dimensional analysis is very limiting for the study of anisotropic seafloors, such as those with oriented sand ripples. A power law has been fitted to rippled seafloor roughness spectra taken along and across the ripple directions by Briggs [15] and the obtained power law parameters were subsequently used in calculations of scattering strength (Jackson and Briggs [16]). A dominant frequency component does not seem to appear in the data. The windowing and averaging operations used in Briggs [15] have the tendency to smear or reduce the frequency resolution, either by averaging adjacent lines in an often non-stationary environment or by the windowing/prewhitening operations (even though the leakage or bias is reduced at higher frequencies). Although the general high frequency trend is fitted by a power law, any small bandwidth components (such as ripples) which may be present are ignored in this type of analysis. Additionally, even if smoothing was not a problem, visual identification of distinct frequency components is hindered by the log-log plots that are normally used to display the spectra. As will be shown in this report, it is the lower-frequency, narrow-bandwidth components that are particularly important in calculations of high frequency subcritical penetration on rippled sand seafloors.

As anisotropic sand seafloors can have rms heights of up to 2 cm or more (Briggs [13], Wheatcroft [14]), theories based on perturbation approximation may not be valid at higher acoustic frequencies, i.e. the criterion $k_1|h(x,y)| << 1$ is not strictly applicable. The model presented in this report uses the Helmholtz-Kirchhoff (H-K) integral with a strict elimination of self-shadowing effects to model the penetration of acoustic energy into the seabed. At high frequency and for relatively smooth seafloors with correlation lengths that are long enough or values of rms roughness that are small enough, the H-K method appears valid. The directionality and three-dimensional distribution of features on the seafloor cannot be ignored and are included in the model by summing contributions from a seafloor surface that is generated using appropriate roughness statistics. As it is the quasi-periodic lower frequency structure that will be most important for the method presented here, a non-centered gaussian is used for constructing realistic seafloor surfaces. The spectrum is also filtered to exclude the non-relevant lowest stochastic scales. Correct beam patterns can be included in order to accurately predict the effect of the plane wave spectrum on subcritical penetration.

The solution for sound penetration presented in this report includes two new components: a more realistic rippled seafloor in conjunction with an improved theory of the acoustic interaction in this type of seafloor. Advantages of the approach used here are that the model is fully three-dimensional, intuitive and accomodating to the evanescent wave and finite beam effects. In Section 2, a discussion of realistic rippled seafloors is presented with their spectra and some examples of generated surfaces. Section 2 also outlines the development of the penetration model. Results of simulations which are run with the system and environmental parameters close to those of Maguer et *al.* [1] are presented in Section 3. These simulations show that the model correctly predicts the frequency at which contributions due to roughness effects begin to dominate those due to the evanescent wave and beam effects, as well as the grazing angle and depth dependence of Bragg interference effects. The last section summarizes the conclusions of the report. A discussion of the validity of the theoretical approach is presented in Annex A.

2

Seafloor interface penetration modeling

The penetration model presented here is based on the Kirchhoff approximation, also called "tangent plane approximation". This approximation assumes that the reflection coefficient and transmission coefficient which are derived for an infinite plane wave encountering an infinite plane surface can be used at every point of a rough surface. Justification of the use of the Kirchhoff approximation for this particular application can be found in Annex A. Briefly, its validity depends on the character of the rough surface in question and whether or not this surface has sharp features. As sandy seafloors are often gently smooth, we will hypothesise that the Kirchhoff approximation is reasonable at low grazing angle even for frequencies as low as 2-3 kHz providing that self-shadowed regions are eliminated from the computation.

The basic principle of the method consists of summing coherently the elementary pressure signals from all the surface points which are not in the shadow regions. Only the points which are "seen" from the source will be the ones which will allow penetration into the sediment (Fig. 1). All the others will be disregarded. The ensemble of contributing interface points may consist of a discontinuous set of small seafloor interface patches. Their size and shape depend directly on the grazing angle and on the seafloor characteristics (rms roughness and correlation lengths mainly).

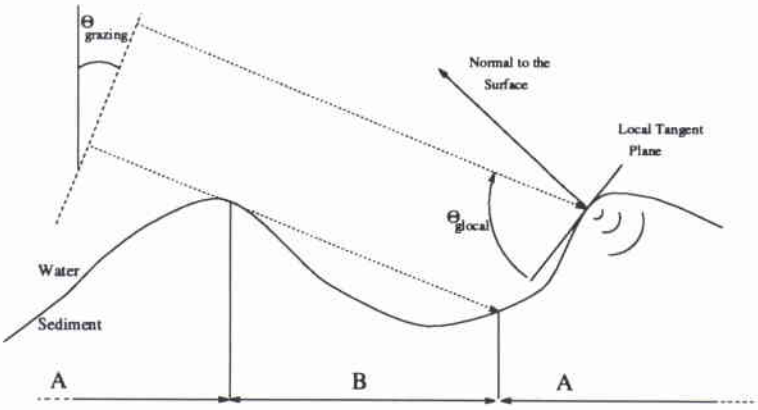

Figure 1 Above and below critical (A) and self shadowing region (B)

2.1 Modeling the seafloor interface

A filtered gaussian spectrum was chosen to describe the rippled seafloor interface. This choice is motivated by the fact that the high frequency region does not have a critical importance as emphasis is on large-scale roughness in the present model. This would not be the case, however, if the approach was based on perturbation theory, which would require accurate estimation of the high frequency part of the spectrum as well. The chosen power spectrum $W_s(\mathbf{K})$ is able to account for either isotropic or non-isotropic features and the general form is expressed analytically as

$$W_s(\mathbf{K}) = Q_s(\mathbf{K}, \mathbf{K_c}) + Q_s(\mathbf{K}, -\mathbf{K_c}). \tag{1}$$

In Eq.(1), the spatial frequency $\mathbf{K_c} = (K_{xc}, K_{yc})$ defines the average ripple wavelength and Q_s, which has the properties of a joint probability distribution function, is given by

$$\begin{aligned} Q_s(\mathbf{K}, \mathbf{K_c}) &= \frac{l_x l_y \eta^2}{4\pi\sqrt{1-\rho^2}} \\ &\quad \times e^{-\frac{l_x^2(K_x-K_{xc})^2 + l_y^2(K_y-K_{yc})^2 - 2\rho l_x l_y (K_x-K_{xc})(K_y-K_{yc})}{2(1-\rho^2)}} && if \quad |\mathbf{K}| > K_{hp} \\ &= 0 && if \quad |\mathbf{K}| \leq K_{hp}, \end{aligned} \tag{2}$$

where K_x, K_y are the components of wavenumber, l_x, l_y are the components of the correlation length. The spatial frequency K_{hp} sets the limit of a high-pass filter that removes very large-scale features and which is necessary for typical seafloors for which low frequency content is absent (e.g. on a very large scale, the seafloor is more or less flat). η is a factor which allows the rms roughness σ_s^2 to be specified independently of K_{hp} or $\mathbf{K_c}$. The parameter ρ is the correlation coefficient between the X and the Y directions and for the sake of simplicity will be set to 0 in this study. Depending on the amplitude of K_c, l_x and l_y, the seafloor can have stronger or weaker directional features. The power spectrum W_s is normalised so that

$$\int_s W_s(\mathbf{K}) d\mathbf{K} = \sigma_s^2. \tag{3}$$

If $\mathbf{K_c} = (\mathbf{0}, \mathbf{0})$ and $l_x = l_y = l$, the seafloor has no directional features and is isotropic and Eq.(2) reduces to the expression:

$$
\begin{aligned}
W_s(K_x,K_y) &= \frac{l^2\eta^2}{2\pi}e^{-\frac{l^2K^2}{2}} && if \quad |\mathbf{K}| > K_{hp} \\
&= 0 && if \quad |\mathbf{K}| \leq K_{hp}.
\end{aligned}
\tag{4}
$$

Figure 2 shows examples of both the anisotropic and isotropic spectra produced with Eqs.(1), (2), and (5). For the isotropic case, η can be related to the rms roughness by the expression:

$$
\eta^2 = \sigma_s^2.e^{\frac{K_{hp}^2 l^2}{2}}. \tag{5}
$$

The spectrum (Eqs.(1) and (2)) is utilized for generating realistic stochastic realisations of the water-sediment interfaces based on the Fourier synthesis method [17]. For each seafloor realisation, a stochastic surface height power spectrum is generated and converted to an amplitude field in the spatial domain using a Fourier transform. Each realisation has the expected first and second moments. The generated power spectrum consists of a pre-defined power roughness spectrum (for example W_s of Eq. (1)) in which part of the phase and the amplitude is randomised. Each random power spectrum produces a unique height field configuration which can be utilised for computing a single realisation of the pressure field at a given location below the generated interface by the method outlined in the next section. Figure 3 is an example of a seafloor interface height field realisation produced by the above method. This surface displays a ripple field which is skewed by 30° with respect to the observer.

2.2 Helmholtz-Kirchhoff formulation

The source is located far from the water sediment interface so that one can assume an effective plane wave insonifying a rough surface with a grazing angle θ_g. In this study, multiple scattering on the water-sediment interface, scattering in the volume and shear waves are not considered. The seafloor volume is considered homogeneous and propagation in the sediment is only affected by the compressional wave attenuation β. Within the restriction on the validity of the Kirchhoff approximation, for a fluid-fluid case, the boundary conditions of pressure and normal velocity continuity across the interface lead to the following relations:

$$
p_t(\mathbf{R}) = [1 + \mathcal{R}_{12}(\mathbf{R_1}, \mathbf{n})]\, p_i(\mathbf{R}). \tag{6}
$$

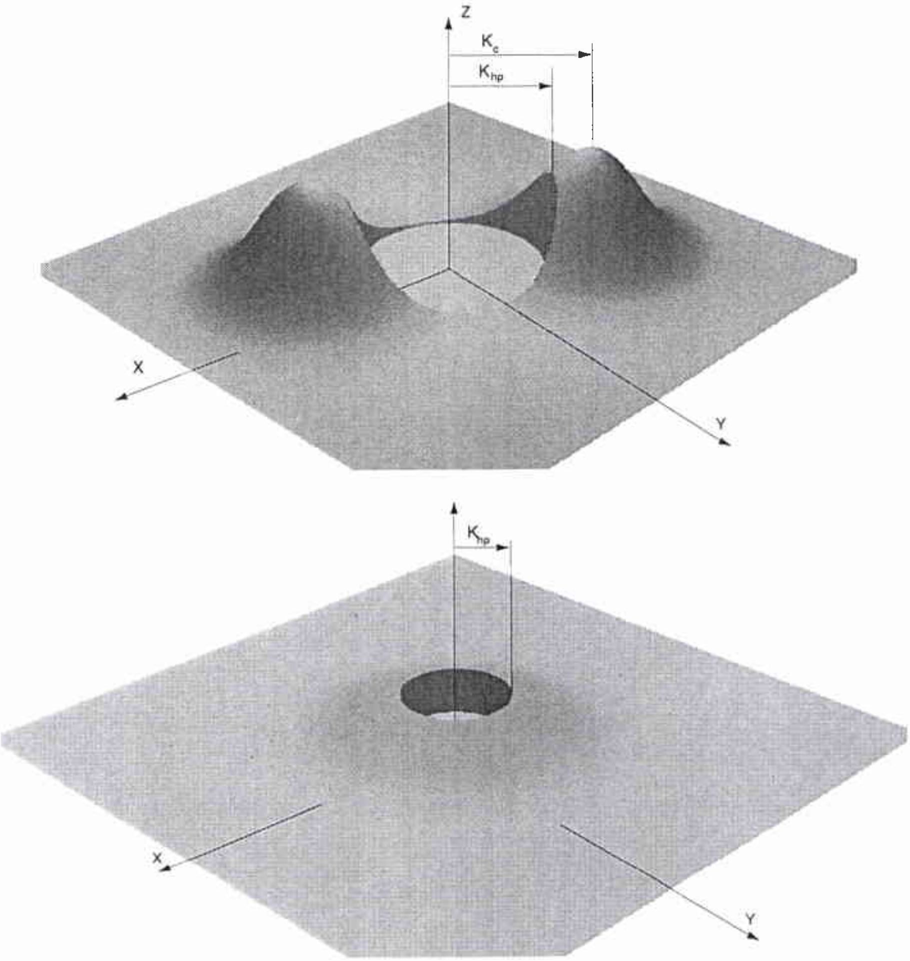

Figure 2 Non isotropic filtered gaussian spectrum (top) and isotropic filtered gaussian spectrum (bottom).

$$\frac{\partial}{\partial n}p_t(\mathbf{R}) = \left[1+\mathcal{R}_{12}(\mathbf{R_1},\mathbf{n})\right]\frac{\partial}{\partial n}p_i(\mathbf{R}). \tag{7}$$

The pressure field $p_i(\mathbf{R})$ is the incoming pressure field in the water at the local point $\mathbf{R}$ (Fig. 4) and $p_t(\mathbf{R})$ represents the pressure field transmitted through the water-sediment interface. The term $(1+\mathcal{R}_{12}(\mathbf{R_1},\mathbf{n}))$ is the local water-sediment plane wave transmission coefficient at the point $\mathbf{R}$. $p_i(\mathbf{R})$ can be expressed in the far field for a slowly varying directivity pattern as:

$$p_i(\mathbf{R}) = p_0 R_0 D_i(\mathbf{R_1}, f) G_i(\mathbf{R_1}), \tag{8}$$

where p_0 is the transmitted pressure level, the term R_0 is a unit of distance and

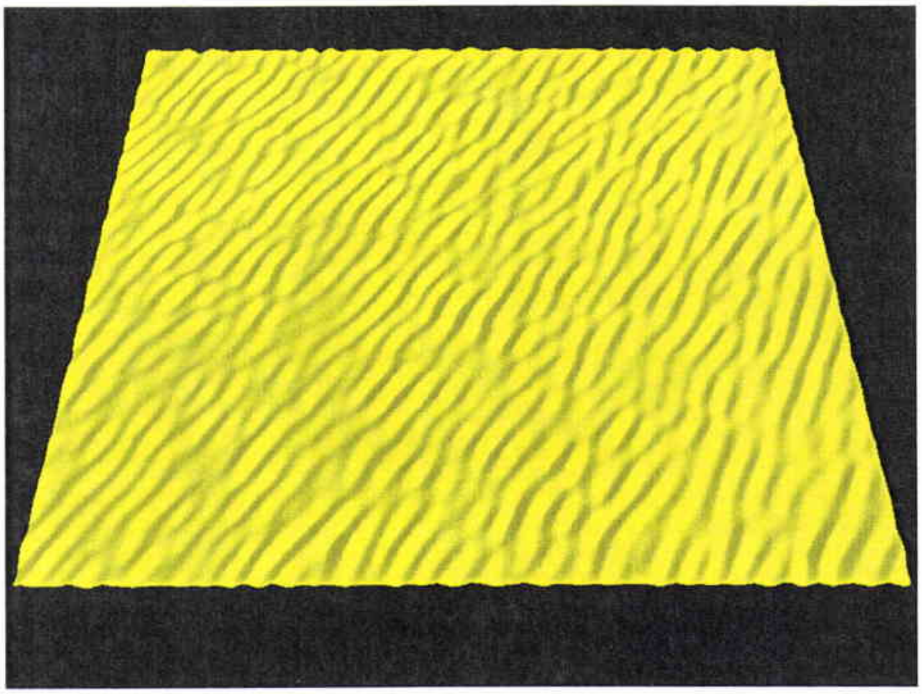

Figure 3 3-D Display of a portion of the seafloor realisation $z(\mathbf{R})$ used in the following simulations. The size of the displayed surface is 6 m x 6 m. On this figure, the rms roughness σ_s^2 is set to 2.5 cm for a better contrast effect, $K_c = 31.5$ rad/m which corresponds to an equivalent ripple wavelength of 20 cm, $K_{hp} = 10$ rad/m. The random generation seed is fixed to 5 and the horizontal spatial sampling is 0.4 cm.

$D_i(\mathbf{R_1}, f)$ is the far field directivity gain in the direction $\mathbf{R_1} = (\mathbf{P} - \mathbf{R})$. This directivity term is assumed to depend on frequency and to be slowly varying with the angle. The term $G_i(\mathbf{R_1})$ is the Green's function for the incident pressure field.

$$G_i(\mathbf{R_1}) = \frac{e^{-j\mathbf{k}_1 \cdot \mathbf{R}_1}}{|\mathbf{R_1}|} = \frac{e^{-jk_1 R_1}}{R_1}, \tag{9}$$

where $R_1 = |\mathbf{R_1}|$. Clay & Medwin [18] propose a formulation of the Helmholtz-Kirchhoff (hereafter refered as H-K) integral for the case of sound penetration through a rough surface when a receiver is located at $\mathbf{R}'$ (see Fig. 4). Here, we consider a differential equation of the H-K formulation by looking at the elementary contribution from an element of surface $d\mathbf{S_R}$ located at the point $\mathbf{R}$ on the interface to the hydrophone located in $\mathbf{R}'$ below this surface. It is assumed that the elementary surface $d\mathbf{S_R}$ located by $\mathbf{R}$ is contained into the contributing surface

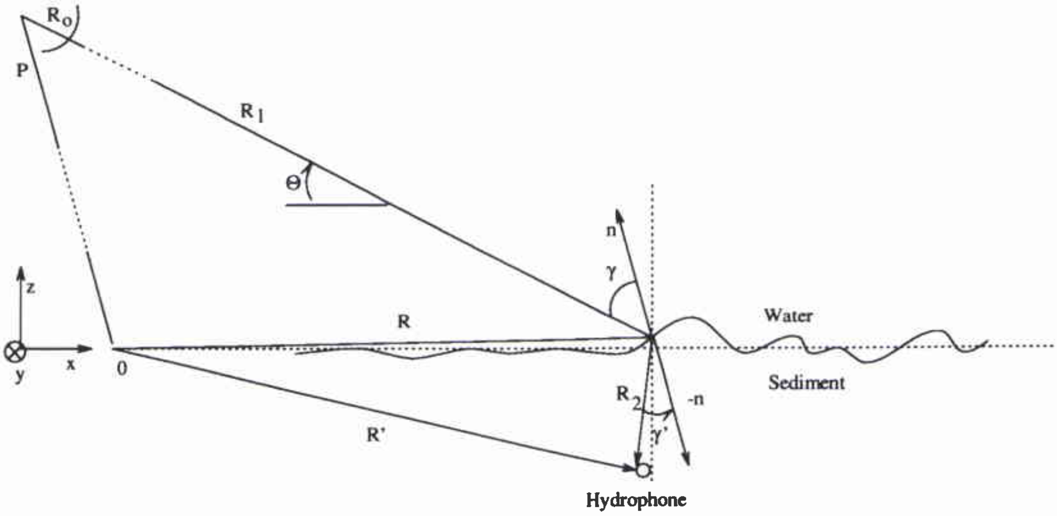

Figure 4 Geometry of measurement. The source is located at **P** and is transmitting an acoustic signal towards the seafloor. A hydrophone is located at $\mathbf{R}'$. **n** is the local normal to the surface.

points S_t:

$$dp(\mathbf{R}') = \frac{1}{4\pi}\left[p_t(\mathbf{R})\frac{\partial}{\partial\mathbf{n}}G_t(\mathbf{R_2}) - G_t(\mathbf{R_2})\frac{\partial}{\partial\mathbf{n}}p_t(\mathbf{R})\right] d\mathbf{S_R}. \tag{10}$$

The operator $\frac{\partial}{\partial\mathbf{n}}$ is a spatial derivative in a direction normal to the surface and $\mathbf{R_2} = |\mathbf{R} - \mathbf{R}'|$. The Green's function $G(\mathbf{R_2})$ of Eq. (10) represents the propagation from the point **R** to the point $\mathbf{R}'$. It can be expressed:

$$G_t(\mathbf{R}, \mathbf{R}') = \frac{e^{-j\mathbf{k_2}.\mathbf{R_2}}}{|\mathbf{R_2}|} = \frac{e^{-jk_1\tilde{n}_2 R_2}}{R_2}. \tag{11}$$

Combining Eqs. (7) and (8), one obtains:

$$\frac{\partial}{\partial\mathbf{n}}p_t(\mathbf{R}) = p_0 R_0 \left[1 + \mathcal{R}_{12}(\mathbf{R_1}, \mathbf{n})\right] D_i(\mathbf{R_1}, f)\frac{\partial}{\partial\mathbf{n}}G_i(\mathbf{R_1}). \tag{12}$$

A closer look at $\frac{\partial}{\partial\mathbf{n}}G_i(\mathbf{R_1})$ shows that:

$$\frac{\partial}{\partial\mathbf{n}}G_i(\mathbf{R_1}) \quad = \quad \nabla.\mathbf{n}[G_i(\mathbf{R_1})]$$

$$= (\frac{\mathbf{R_1}.\mathbf{n}}{|\mathbf{R_1}|})\frac{\partial}{\partial R_1}\left(\frac{e^{-jk_1R_1}}{R_1}\right). \tag{13}$$

It is assumed that $k_1R_1 \gg 1$ (source far from the interface). We can then approximate (13) by:

$$\begin{aligned}\frac{\partial}{\partial \mathbf{n}}G_i(\mathbf{R_1}) &= -(\frac{\mathbf{R_1}.\mathbf{n}}{|\mathbf{R_1}|})jk_1G_i(\mathbf{R_1})\\ &= j\cos(\gamma(\mathbf{R_1},\mathbf{n}))k_1G_i(\mathbf{R_1}).\end{aligned} \tag{14}$$

with $(\frac{\mathbf{R_1}.\mathbf{n}}{|\mathbf{R_1}|}) = -\cos(\gamma(\mathbf{R_1},\mathbf{n}))$ and $\gamma(\mathbf{R_1},\mathbf{n})$ being the angle between the incident direction and the normal vector $\mathbf{n}$ to the surface at $\mathbf{R}$. The second term in the bracket of the right hand side of (10) then equals:

$$-G_t(\mathbf{R_2})\frac{\partial}{\partial n}p_t(\mathbf{R}) = -j\cos(\gamma(\mathbf{R_1},\mathbf{n}))k_1p_t(\mathbf{R})G_t(\mathbf{R_2}). \tag{15}$$

In the same way:

$$p_t(\mathbf{R})\frac{\partial}{\partial n}G_t(\mathbf{R_2}) = -(\frac{\mathbf{R_2}.\mathbf{n}}{|\mathbf{R_2}|})(jk_2 + \frac{1}{R_2})p_t(\mathbf{R})G_t(\mathbf{R_2}). \tag{16}$$

Assuming that $k_2R_2 \gg 1$ which is the case if we consider the hydrophone sufficiently far from the water-sand interface, we obtain:

$$p_t(\mathbf{R})\frac{\partial}{\partial n}G_t(\mathbf{R_2}) = -j\cos(\gamma'(\mathbf{R_2},-\mathbf{n}))k_1\bar{n}_2p_t(\mathbf{R})G_t(\mathbf{R_2}). \tag{17}$$

Then, combining (15), (17) and (10),

$$\begin{aligned}dp(\mathbf{R'}) &= -\frac{jk_1}{4\pi}p_0R_0D_i(\mathbf{R_1},f)\,[1+\mathcal{R}_{12}(\mathbf{R_1},\mathbf{n})]\,G_i(\mathbf{R_1})G_t(\mathbf{R_2})\\ &\times\ [\cos(\gamma(\mathbf{R_1},\mathbf{n})) + \bar{n}_2\cos(\gamma'(\mathbf{R_2},-\mathbf{n}))]\,d\mathbf{S_R}.\end{aligned} \tag{18}$$

For a non-CW signal of spectrum $E(f)$, grouping together all the frequency dependent terms, equation (19) becomes:

$$\begin{aligned} dp(\mathbf{R}', f) &= -\frac{j}{2c_1} p_0 R_0 \left[1 + \mathcal{R}_{12}(\mathbf{R_1}, \mathbf{n})\right] \left[\cos(\gamma(\mathbf{R_1}, \mathbf{n})) + \bar{n_2} \cos(\gamma'(\mathbf{R_2}, -\mathbf{n}))\right] \\ & \quad \times \left[f.E(f) D_i(\mathbf{R_1}, f) G_i(\mathbf{R_1}) G_t(\mathbf{R_2})\right] d\mathbf{S_R}. \end{aligned} \tag{19}$$

Here, we assume that the reflection coefficient does not depend on frequency over the considered bandwidth. The average index of refraction $\bar{n_2}$ has to be considered as a complex entity as the sediment is assumed to be dissipative:

$$\bar{n_2} = \bar{n_2'} - j\bar{n_2''}. \tag{20}$$

Expressing the Green function, one obtains:

$$\begin{aligned} dp(\mathbf{R}', f) &= -\frac{j}{2c_1 R_1 R_2} p_0 R_0 \left[1 + \mathcal{R}_{12}(\mathbf{R_1}, \mathbf{n})\right] \left[\cos(\gamma(\mathbf{R_1}, \mathbf{n})) + \bar{n_2} \cos(\gamma'(\mathbf{R_2}, -\mathbf{n}))\right] \\ & \quad \times \left[f.E(f) D_i(\mathbf{R_1}, f) e^{-jk_1(R_1 + \bar{n_2'} R_2)} e^{-k_1 \bar{n_2''} R_2}\right] d\mathbf{S_R}, \end{aligned} \tag{21}$$

and if we consider that the attenuation β in the seafloor is frequency dependent, we have:

$$\beta = \alpha |f| = 2k_1 \bar{n_2''}, \tag{22}$$

where α is the attenuation coefficient which is assumed to be fixed at a given sediment porosity. Transforming to time domain, using the inverse Fourier transform, we obtain:

$$\begin{aligned} dp(\mathbf{R}', t) &= \mathcal{F}^{-1}\{dp_{(S)}(\mathbf{P}', \mathbf{f})\} \qquad (23) \\ &= -\frac{j}{2c_1 R_1 R_2} p_0 R_0 \left[1 + \mathcal{R}_{12}(\mathbf{R_1}, \mathbf{n})\right] \left[\cos(\gamma(\mathbf{R_1}, \mathbf{n})) + \bar{n_2} \cos(\gamma'(\mathbf{R_2}, -\mathbf{n}))\right] \\ & \quad \times \mathcal{F}^{-1} \left[f.E(f) D_i(\mathbf{R_1}, f) e^{-jk_1(R_1 + \bar{n_2'} R_2)} e^{-\frac{\alpha |f| R_2}{2}}\right] d\mathbf{S_R}. \end{aligned}$$

Considering that:

$$
\begin{aligned}
\mathcal{F}^{-1}\left[f.E(f)e^{-jk_1(R_1+\bar{n}_2' R_2)}e^{-\frac{\alpha|f|R_2}{2}}D_i(\mathbf{R_1},f)\right] &= \\
& \quad \mathcal{F}^{-1}\left[f.E(f)e^{-jk_1(R_1+\bar{n}_2' R_2)}\right] \\
& * \quad \mathcal{F}^{-1}\left[e^{-\frac{\alpha|f|R_2}{2}}\right] \\
& * \quad \mathcal{F}^{-1}\left[D_i(\mathbf{R_1},f)\right],
\end{aligned}
\tag{24}
$$

following [19]:

$$
\mathcal{F}^{-1}\left[f.E(f)e^{-jk_1(R_1+\bar{n}_2' R_2)}\right] = \frac{1}{2\pi j}e'(t-\frac{R_1+\bar{n}_2' R_2}{c_1}).
\tag{25}
$$

and thus, Eq. (24) can be expressed as:

$$
\begin{aligned}
dp(\mathbf{R}',\mathbf{t}) &= \mathcal{F}^{-1}\left[dp_{(S)}(\mathbf{P}',\mathbf{f})\right] \\
&= \frac{p_0 R_0}{4\pi c_1 R_1 R_2}\left[1+\mathcal{R}_{12}(\mathbf{R_1},\mathbf{n})\right]\left[\cos(\gamma(\mathbf{R_1},\mathbf{n}))+\bar{n}_2\cos(\gamma'(\mathbf{R_2},-\mathbf{n}))\right] \\
& \times e'(t-\frac{R_1+\bar{n}_2' R_2}{c_1}) * \mathcal{F}^{-1}\left[e^{-\frac{\alpha|f|R_2}{2}}\right] * \mathcal{F}^{-1}\left[D_i(\mathbf{R_1},f)\right] d\mathbf{S_R}.
\end{aligned}
\tag{26}
$$

Computing the total pressure field received at the hydrophone consists of summing all the elementary pressures $dp_{(S)}(\mathbf{P}',\mathbf{t})$ over the surface (S_t) which is allowing penetration:

$$
p(\mathbf{R}',t) = \int_{(S_t)} dp(\mathbf{R}',\mathbf{t}).
\tag{27}
$$

The computation of $p(\mathbf{R}',t)$ of Eq. (27) is based on the stochastic realisation of seafloor interface height fields $z(\mathbf{R})$ presented in section 2.1.

2.3 Self-shadowing removal

Self-shadowing and multiple scattering have a relative greater effect on scattering at low grazing angle for gently ondulating surfaces. Regarding the self-shadowing effect, the number and the size of the patches which are masked and not "seen" from the source increase as seafloor rms roughness increases and as the grazing angle decreases. Including these surface points in the Helmholtz-Kirchhoff integral is obviously not correct (see Fig. 1). This is one of the reasons why the Helmholtz-Kirchoff integral is often considered to be an invalid method for solving scattering at low grazing angle. Any solution of this integral over the whole surface (including self-shadowed points) requires the addition of a self-shadowing correction term [20] which may not account properly for the actual self-shadowing effect. In this particular approach, an artificial height field having the expected first and second moments is generated and for a given geometrical configuration, it is possible to locate exactly every point of the generated seafloor that is self-shadowed. These points are systematically removed from the ensemble of surface points S on which the H-K integral is performed.

At these low grazing angles, the transversal component of the incoming rays is very small compared to the forward component $\mathbf{R_{1x}}$ if the source is sufficiently far from the considered surface. Therefore, the shadow detection algorithm is performed by using a one-dimensional algorithm in the x direction on the generated surface. Figure 5 shows the evolution of the self-shadowed surface patches as the grazing angle decreases from 30° to 15° for a 1 cm rms rough surface. About 3% of the seafloor is self-shadowed at 30° whereas more than 15% is masked at 15°. The size and number of shadowed areas are even greater for higher roughnesses. Even at 25°, the self-shadowing regions are large enough to have a considerable effect on penetration and should be taken into account in any model of penetration.

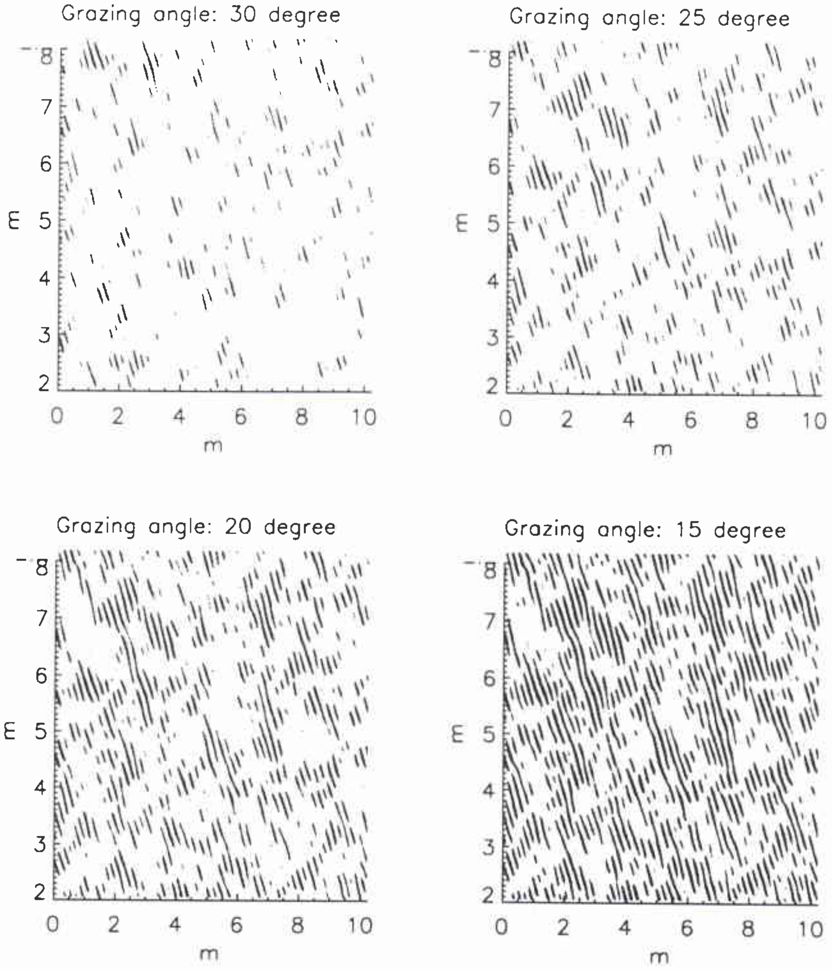

Figure 5 Evolution of the self-shadowed surface size as the grazing angle decreases on a portion (6m x 10 m) of the generated height field displayed in Fig. 3. Masked areas are in black. Source height is set constant at 8 m on the left as regards to the insonified surface. Top left: distance from the source $R_1 = 16$ m $\theta_g = 30°$, 2.55% shadow coverage, Top right: distance from the source $R_1 = 18.93$ m $\theta_g = 25°$, 5.29% shadow coverage, bottom left: $R_1 = 23.39$ m, $\theta_g = 20°$, 9.92% shadow coverage, bottom right: $R_1 = 30.91$ m, $\theta_g = 15°$, 16.78% shadow coverage. $K_c = 31.5$ rad/m, $\sigma_s = 1$ cm, $K_{hp} = 10$ rad/m, seed = 5.

3

Penetration model simulations

3.1 Definition of the penetration ratio

It is necessary to define entities that quantify the penetration of sound waves into the sediment. For a transmitted pulse of spectrum $E(f)$, the energy received at the hydrophone buried into the sediment at frequency f can be expressed as:

$$E_{bh}(f) = \frac{1}{\bar{\rho_2}\bar{c_2}} p(\mathbf{R}', f) p^*(\mathbf{R}', f), \tag{28}$$

where $\bar{\rho_2}$ is the average density of sand. The received energy just above the surface has this expression:

$$E_{ph}(f) = \frac{1}{\rho_1 c_1} (\frac{p_0^2 R_0^2}{R_1^2} D_i^2(\mathbf{R_d}) E^*(f) E(f)), \tag{29}$$

where ρ_1 is the average density of sea water. The vector $\mathbf{R_d}$ will be picked as being directed towards the surface point for which the directivity pattern is maximum , so that $D_i(\mathbf{R_d}) = 1$. We define the penetration ratio as:

$$PR(f) = 10 \log_{10}(E_{bh}(f)/E_{ph}(f)) + 10 \log_{10}(\frac{\bar{\rho_2}\bar{c_2}}{\rho_1 c_1}). \tag{30}$$

The definition of $PR(f)$ is not an energy ratio. It corresponds to the transfer function of the water-sand interface. In order to obtain an energy ratio, the term $10 \log_{10}(\frac{\bar{\rho_2}\bar{c_2}}{\rho_1 c_1})$ can be removed from Eq. 30 which results in subtracting about 6 dB from the $PR(f)$ in the case of a sandy seabed. Finally, the total penetration ratio over the whole bandwidth is defined as follows:

$$TPR = 10 \log_{10} \left[\int_{-\infty}^{\infty} PR(f) df \right]. \tag{31}$$

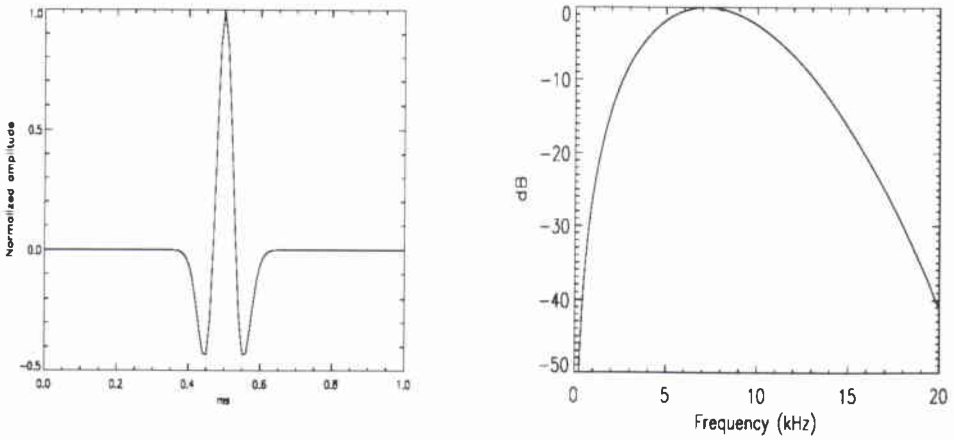

Figure 6 Ricker signal $e(t)$ used in the simulation (left) and it corresponding power spectrum (right).

The values of the TPR are strongly sensitive to the hydrophone position. As observed at sea and with the model simulation, the position of the hydrophone greatly affects E_{bh}, $PR(f)$ and TPR. Thus, reference to a nominal grazing angle θ_g without specifying the exact location of the hydrophone below the seafloor interface may lead to unexpected penetration levels. Sensitivity to the hydrophone position is discussed later in this report.

At sea experiments performed by Maguer *et al.* [1] in the Gulf of Biodola (island of Elba, Italy) used a constant source height (see Fig. 4) with respect to the average seafloor level. This source is positioned on a tower which can be moved horizontally on a rail in the $X-$ direction. As the range between the source and the hydrophone changes, the grazing angle also changes which affects the size of the insonified seafloor patch and also influences the amount of sound penetration. The sensitivity of penetration levels to system geometry emphasizes the need to control the geometry parameters at sea as well as in simulations. This is particularly crucial around and below the critical angle where penetration levels vary strongly with angle.

3.2 Example of penetration above and below critical angle

The transmitted signal used in the simulation is a theoretical Ricker pulse centred around 8 kHz. Figure 6 shows the signal and its corresponding power spectrum. This wideband signal has however little energy below 2 kHz and above 15 kHz and as a consequence, apart from the problem of validity of the present model as frequency goes down, simulated penetration ratios may be inaccurate below 2 kHz.

Figure 7 presents model predictions of the amount of energy received at 8kHz by the hydrophone located 30 cm underneath the centre of the seafloor surface. A directivity pattern close to the one of the parametric source used by Maguer [1] for a 8kHz Ricker pulse is used here. The generated seafloor surface is the same used to illustrate the effect of the self-shadowing effect on Fig. 5. The energy pattern shows that most of the energy comes from the area directly above the hydrophone. The energy patch spreads out as the grazing angle decreases. The directionality of the surface ripples tends to enhance the energy contribution in the left bottom area of the surface.

Figure 8 presents a series of simulated signals received in the sediment above and below critical incidence. Similarly to at sea measurements during the penetration experiment by Maguer [1], the water sound speed is taken as 1530 m/s and the sediment sound speed as 1685 m/s which corresponds to a critical angle of 24.8°. The generated surface used for these simulations is the surface presented in Fig. 3, Fig. 5 and Fig. 7. The hydrophone is located vertically 30 cm below the intersection of the centre of the beam and the zero level of the surface (Fig. 8 (top)). It is interesting to observe that the received signals are mostly coherent above and even at the critical angle. As the grazing angle decreases, the coherence is degraded but, as low as 20°, the initial part of the received signals remains quite close to the transmitted pulse shape. Below 20°, the coherence deteriorates because the rough character of the surface starts playing a dominant role. It becomes almost impossible to distinguish a shape similar to the transmitted pulse in the received signal at 15°. The bottom of Fig. 8 presents the same series of simulated signals for a hydrophone located 60 cm below the water-sand interface. As for a hydrophone located 30 cm below the interface, the coherence is good above the critical angle. But below 20°, the first part of the signal is even more strongly attenuated than at 30 cm.

Figure 9 shows the penetration ratios corresponding to the signals displayed in Fig. 8. The penetration ratios change significantly from 30° to 15°. From a quasi constant level of $PR(f)$ at 30° which reveals a relatively weak dependence of the penetration on roughness and an expected dependence on attenuation, the penetration ratio begins to display an interference structure as the grazing angle decreases. These interference minima do not appear to be located randomly. As the grazing angle decreases, the minima and maxima are shifted down in frequency which is in accordance with the Bragg theory as the surface used here contains periodical features: the average correlation length is centred around 20 cm and is skewed by 30° away from the Y-axis. This corresponds to an equivalent correlation length of 23 cm in the X direction. But classical Bragg theory computation on the location of minima and maxima is not consistent on Fig. 9 between the case at 30 cm and the case at 60 cm. Considering the sole interference mechanism produced in the water medium, the locations of the minima and maxima present on Fig. 9 for a burial depth of 60 cm are not in accordance with those for a burial depth of 30 cm. This suggests that the interference phenomenon is not only occurring in the upper medium but also inside the seafloor and that the hydrophone position is a key factor in the construction of interference fringes; for a given location $\mathbf{R}'$ of the hydrophone, there exists a set of frequencies for which constructive and destructive interference will occur. This phenomenon is not easily quantifiable at sea, but an important difference in the spectral signature of $PR(f)$ has been observed at sea for hydrophones located 50 cm apart [1]. Figures 10 and 11 illustrate this phenomenon. On Fig. 10, at 30° grazing angle (i. e. above critical), the interference patterns change slowly because the roughness effect is dominated by classical refraction mechanisms. As the hydrophone position increases in the X-direction, penetration increases because the hydrophone is closer to the main direction of the refracted rays into the sediment. On Fig. 10(b), below critical, the penetration ratio is more sensitive to the hydrophone position. This is because below critical, the evanescent wave is only dominant in the lower frequency region, leaving the roughness as the dominant effect above 3 kHz in this case where the importance of the hydrophone position is particularly critical. Figure 11 shows a decay of the TPR below critical as the hydrophone moves away from the source. This can be explained by an increasing distance of the hydrophone from the location on the water-sand interface where acoustic rays coming from the source $\mathbf{P}$ are interacting with the water-sand interface at higher grazing angles. This is also due to the limited size of the insonified footprint in this particular example. This confirms the importance of the hydrophone location reative to the seafloor height field as well as the particular realisation of that seafloor height field.

3.3 Parametrisation with rms roughness

The effect of roughness on the total penetration ratio both 30 cm and 60 cm below the interface is shown in Fig. 12. Contrary to the case of a flat seafloor ($\sigma_s = 0$), for which, according to classical theory (e. g. evanescent wave), penetration decreases regularly as the grazing angle decreases, simulations of $PR(f)$ on a rough surface show that seafloor roughness plays a significant role on the penetration level above and below critical angle. Above critical angle, because of the classical refraction effect, roughness tends to reduce the penetration level whereas below critical angle, local facet orientation facilitates penetration. In addition to this effect, increase of self-shadowing as rms roughness increases, tends to slightly reduce penetration in the 10 – 20° grazing angle range (Fig. 12). These two effects are more noticeable at 60cm where the evanescent wave component becomes weaker. At 15°, there is a 6 dB increase of energy at 30 cm and about 12 dB increase at 60 cm. This anomalous penetration is important in terms of total energy level but as its content is primarily incoherent, as grazing angle goes down, its interest for detection is open to discussion.

Figure 13 presents an example of the sensitivity of the penetration ratio to the rms roughness at various grazing angles. The solid lines correspond to a non-rough seafloor and thus are the results of the coupling of the evanescent component with the plane wave spectrum effect [6]. For non-zero roughnesses, it is interesting to observe that the amplitude of the rms roughness does not seem to strongly affect the penetration ratio. At some frequencies, interference fringes are amplified or diminished (by a few dB), but there is very little change in term of average energy between 1 cm rms height and 2 cm rms height (see Fig. 12). On the contrary, simulations not displayed here show that the horizontal statistics (mainly the correlation length and the ripple orientation) greatly affect the spectral signature of the received signal by modifying the interference pattern and the amplitude of the penetration ratio. However, the TPR is not significantly affected for various horizontal configurations.

3.4 *Sensitivity of the penetration ratio to seafloor realisations*

As suggested in section 3.2, it is not only the position of the hydrophone but also the seafloor height field realisation which greatly affect the scattered component of the received pressure field into the seafloor. Figure 14 shows that each seafloor realisation having the same exact statistical characteristics produce a very different penetration ratio. This suggests also that the scattering field is completely incoherent as opposed to the evanescent field and non uniformly distributed in space. At a given frequency, the standard deviation can be large (about $\pm 10dB$).

3.5 *Influence of roughness anisotropy*

Intuitively, a variation of the incoherent field as the ripple orientation changes is expected. Figure 15 shows that insonification of the seafloor across the ripple field will produce more interference pattern and higher variance of the scattered field around the coherent field. Along the ripples (90°), the scattered field is almost null as if the ripple field was not “seen” by the incident sound waves. Between these two extreme case, there is a gradual change in the variance of the scattered field. It is interesting to notice that the total penetration ratio (not displayed here) is quasi constant as the ripple orientation changes both below and above critical. Below critical, there is only a 3dB excess of incoherent energy that penetrates the seafloor across the ripples (0°) compared to the case along the ripples (90°). Above critical, the total penetration ratio is constant to within one dB.

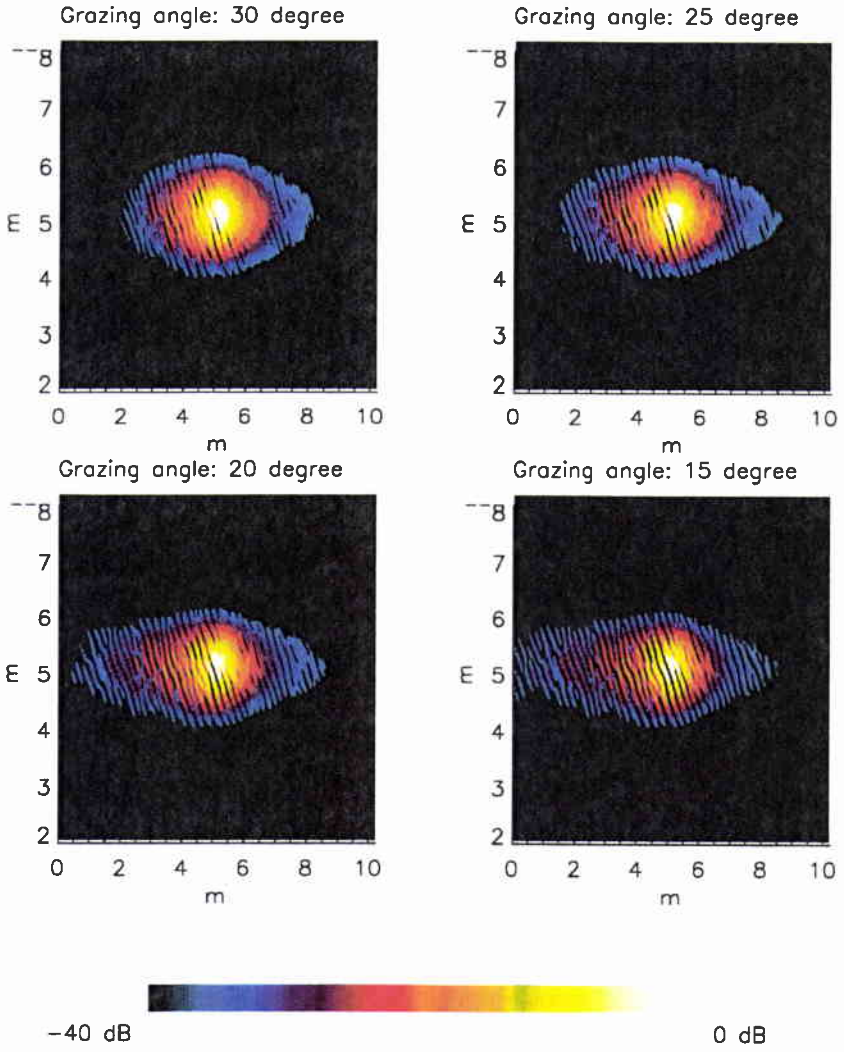

Figure 7 Energy contributions from the S_t ensemble of points from Fig. 3 and Fig. 5 at 4 different grazing angles at a center frequency of 8 kHz. The source beam is pointing towards the centre of each image The source is located on the left. A theoretical square gaussian source of width $(2\theta_{3dB} = 6°)$ is picked. $\bar{c_1} = 1530$ m/s, $\bar{c_2} = 1685$ m/s, $\bar{\rho_2} = 1.8\text{g/cm}^3$, $\alpha = 0.8$ dB/m/kHz. The hydrophone is located 30 cm vertically below the very centre of the height field. Top left: distance from the source $R_0 = 16$ m $\theta_g = 30°$, Top right: distance from the source $R_0 = 18.93$ m $\theta_g = 25°$, bottom left: $R_0 = 23.39$ m, $\theta_g = 20°$, bottom right: $R_0 = 30.91$ m, $\theta_g = 15°$. $K_c = 31.5$ rad/m, $\sigma_s = 1$ cm, $K_{hp} = 10$ rad/m, skewness = 30°, seed = 5.

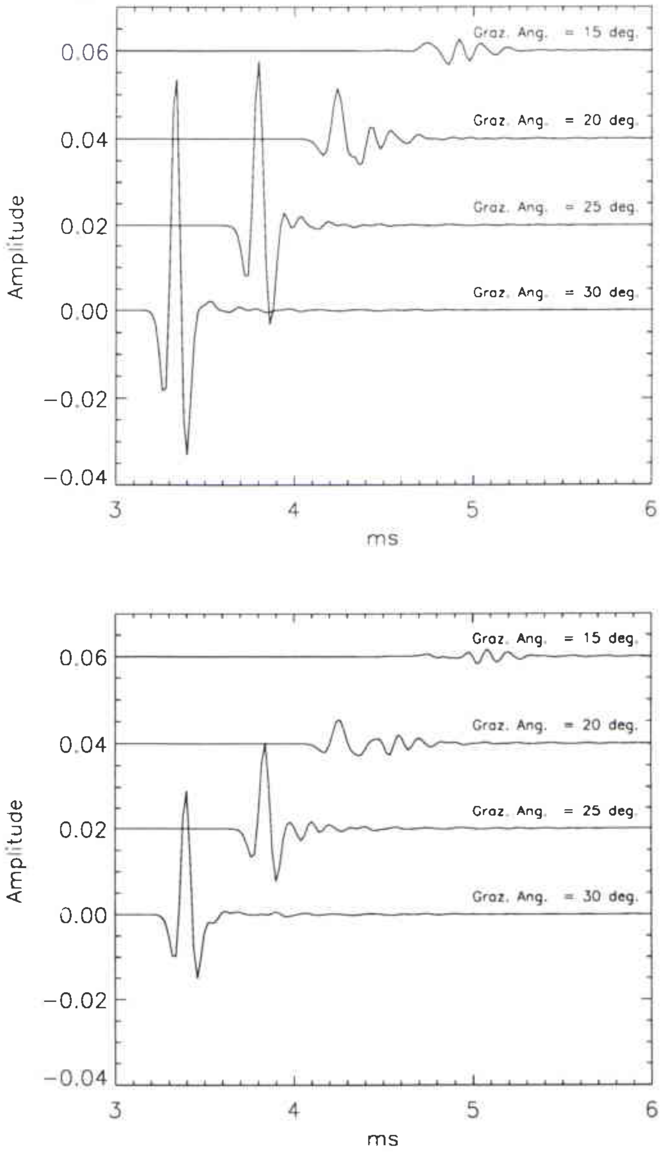

Figure 8 Example of received pressure signals $p(\mathbf{R}', t)$ vs. time at various grazing angles. The input parameters are the ones used for simulation of Fig. 7. The time origin and the amplitude factor are arbitrary but kept constant for the 4 signals. The main direction of the source beam is pointing towards the centre of the height field. A theoretical square gaussian source of width ($2\theta_{3dB} = 6°$) is picked. The hydrophone is located 30 cm (top figure) and 60 cm (bottom figure) down into the seafloor. $K_c = 31.5$ rad/m, $\sigma_s = 1$ cm, seed = 5

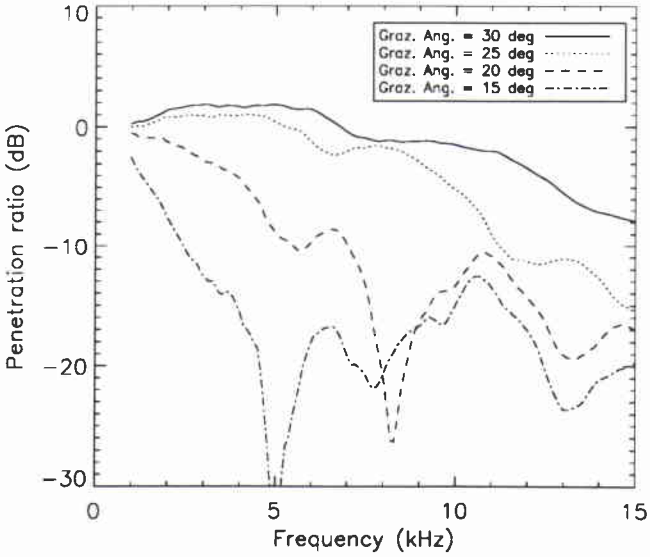

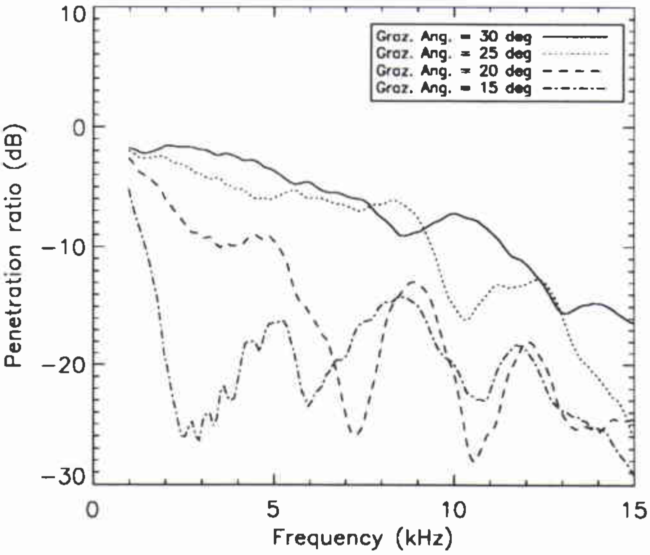

Figure 9 Example of the penetration ratio $PR(f)$ at various grazing angles. The present penetration ratios correspond to the signals of Fig. 8, for a hydrophone buried 30cm (top) and 60 cm (bottom) into the seabed.

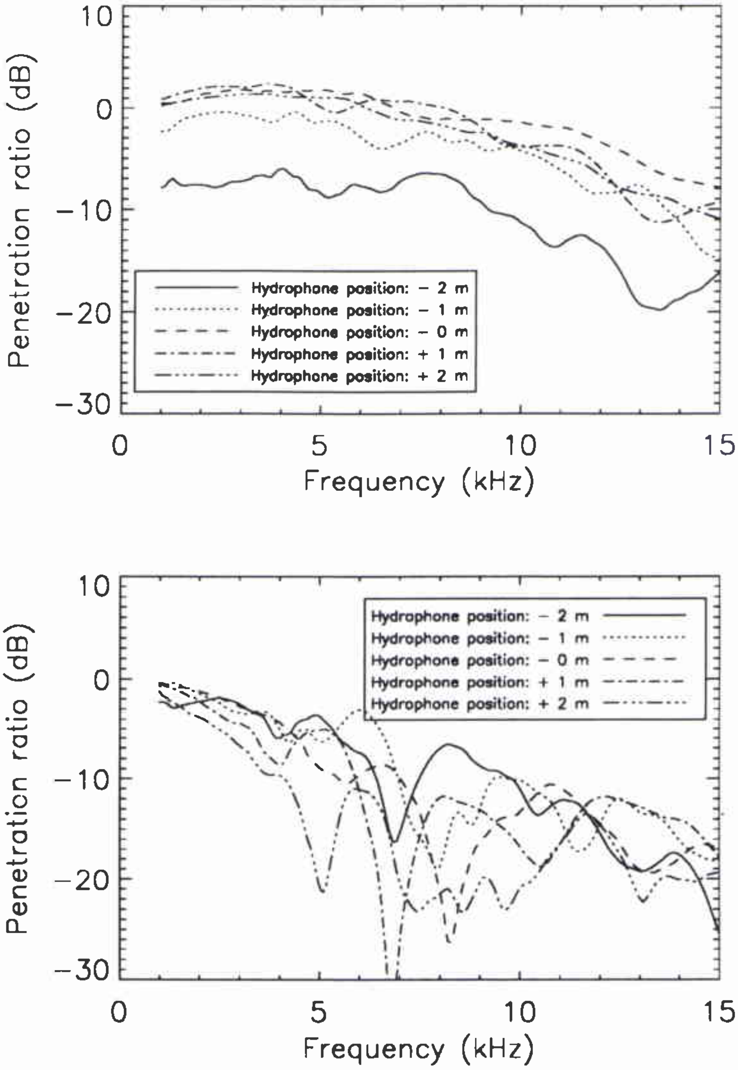

Figure 10 Example of the variability of the penetration ratio $PR(f)$ for various horizontal positions of the hydrophone. The hydrophone is located in the plane OXZ. Hydrophone position $\mathbf{R}' = (x, 0, -30\text{cm})$. Top: $\theta_g = 30°$. Bottom: $\theta_g = 20°$. All other geometric and geoacoustic parameters are the same as on the previous figures.

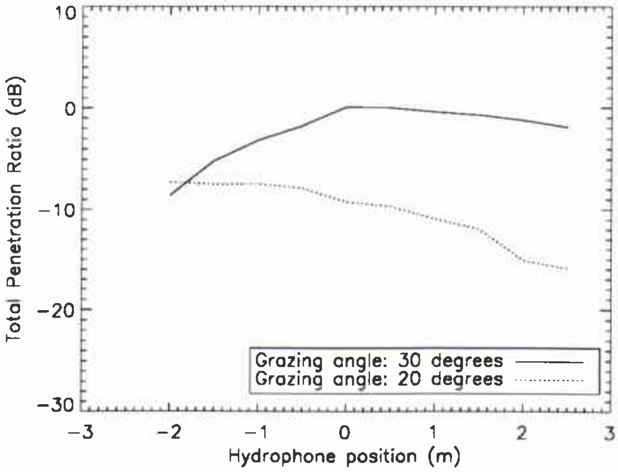

Figure 11 Total penetration ratio $TPR(f)$ versus the hydrophone horizontal position at two distinct grazing angle (30° and 20°).

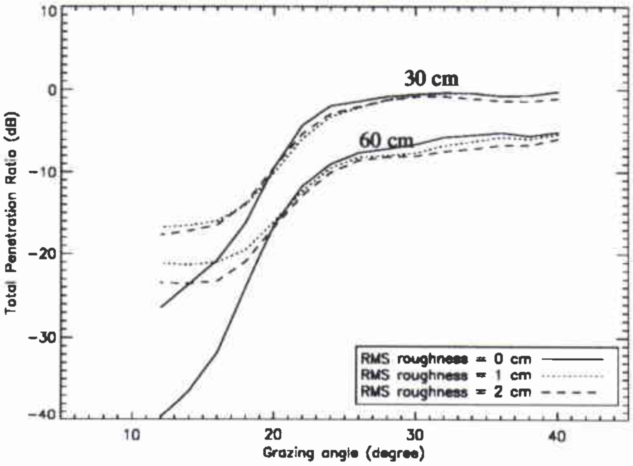

Figure 12 Total penetration ratio (TPR) vs the grazing angle for various roughnesses and two hydrophone burial depth from cases presented on Fig. 8 and Fig. 9.

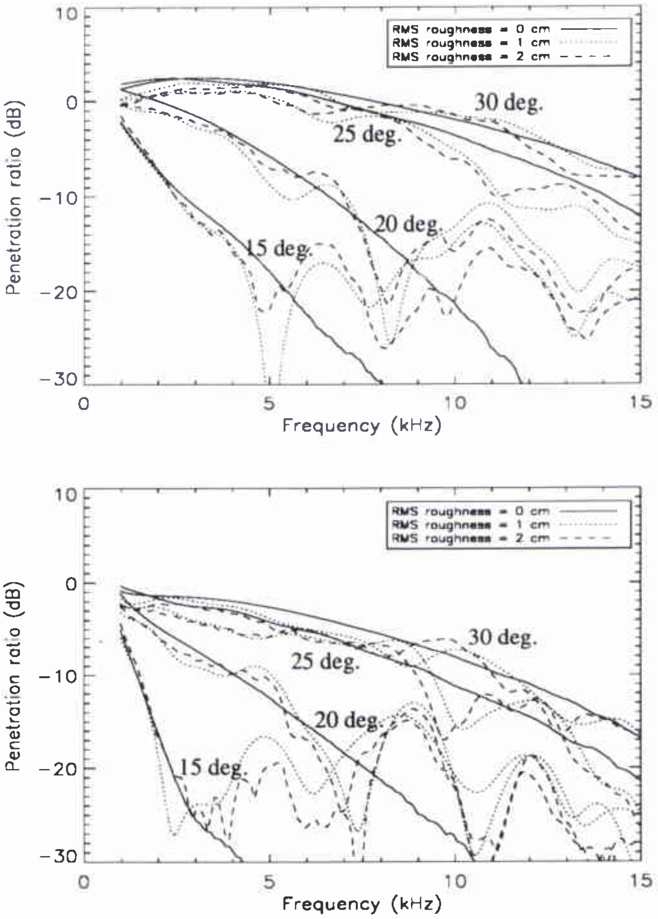

Figure 13 Penetration ratio PR(f) for various grazing angles and various roughnesses (0,1,2 cm rms). The hydrophone is buried 30 cm (top figure) and 60 cm (bottom figure) into a sandy sediment. The geometrical and geoacoustical conditions are the same as the previous simulations.

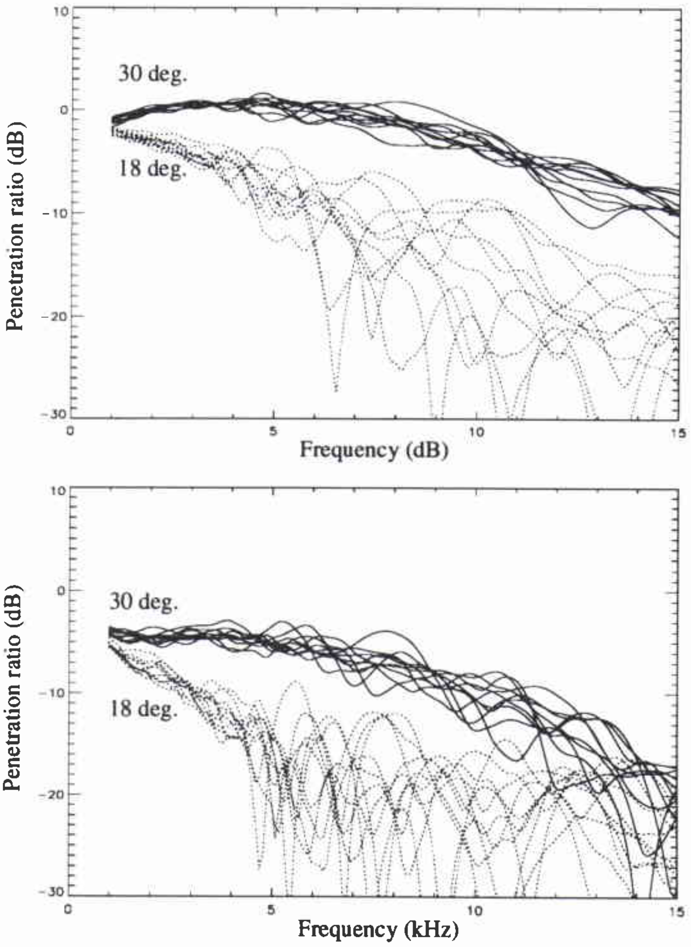

Figure 14 Example of the sensitivity of the penetration ratio PR(f) for 10 realisations of the seafloor having the same statistics: 30 cm burial depth (top), 60 cm burial depth (bottom). $Kc = 31.5$ rad/m, $\sigma_s = 1$ cm. $c_1 = 1530$ m/s, $\bar{c}_2 = 1685$ m/s.

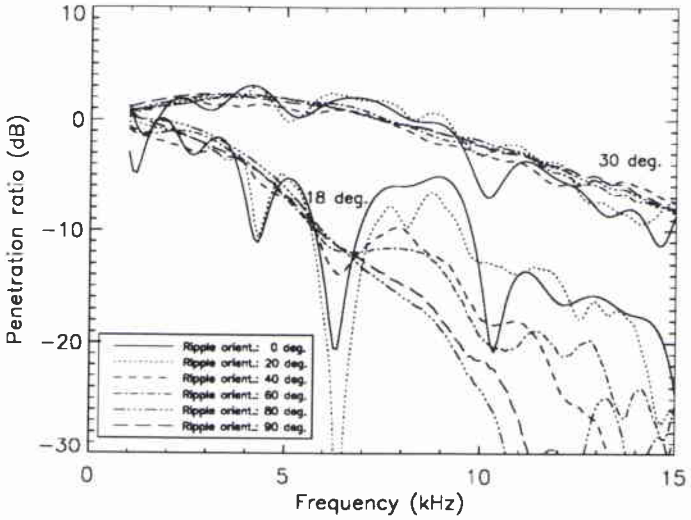

Figure 15 Example of the variability of the penetration ratio $PR(f)$ for various orientations of the same ripple field (0° corresponds to an insonification across the ripple edges, 90° is alongside) above critical (top set of curves) and below critical (bottom set of curves). The geometric and geoacoustic parameters are the same as on the previous figures.

4

Summary

A Helmholtz–Kirchhoff (H-K) model of the penetration of sound into sandy seafloors has been presented. The model addresses in particular the effects of seabed roughness with particular attention being given to simulation of the sea floor spectrum. The model is restricted by the usual H-K assumptions (e.g. no sharp edges, large radii of curvature compared to the wavelength, etc.) but remains valid over the frequency range and the parameters relevant in the experiment by Maguer on rippled seabeds. The model demonstrates that, as the acoustic frequency increases, the importance of the evanescent wave decreases with concomitant increased importance of roughness scatter in contributing to an explanation of sound penetration into the seabed at grazing angles beyond 'critical' . As such studies show good agreement with the experiment, the model may be used with confidence in a survey of likely effects due to ripple heights and orientations.

5

Acknowledgments

The authors wish to thank Alain Maguer, Edoardo Bovio, Warren Fox, John Osler, Henrik Schmidt and Finn Jensen for their helpful comments in the discussions about acoustic seabed penetration.

References

[1] A. Maguer, E. Bovio, W.L.J. Fox, E. Pouliquen, H. Schmidt, "Mechanisms for subcritical penetration into a sandy bottom: experimental and modeling results", SACLANTCEN, SR-287, April 1998.

[2] N.P. Chotiros, "Biot model of sound propagation in water-saturated sand", *Journal of the Acoustical Society of America* Vol. 97, pp 199-214, January 95.

[3] N.P. Chotiros, A. M. Mautner, A, Lovik, A. Kristensen, O. Bergem, "Acoustic penetration of a silty sandsediment in the 1-10kHz band", *Journal of Oceanic Engineering* Vol. 22, pp 602-615, Oct 1997.

[4] J.L. Lopes, "Observation of anomalous acoustic penetration into sediment at shallow grazing angles", *Journal of the Acoustical Society of America* Vol. 99, pp 2473-2474, April 1996.

[5] J.C. Olser, A.P. Lyons, E. Pouliquen, " A field study on the penetration of acoustic energy into sand seabed", SACLANTCEN, SM-338, May 98.

[6] F.B. Jensen, H. Schmidt, "Subcritical penetration of narrow gaussians beams into sediment", *Journal of the Acoustical Society of America* 82 (1), 574-759, August 1987.

[7] K.L. Williams, L.J. Satkowiak, D.R. Bugler "Linear and parametric array transmission across a water-sand interface - Theory, experiment, and observation of beam displacement", *Journal of the Acoustical Society of America* Vol. 86(1), pp 311-325, July 1989.

[8] E.I. Thorsos, D.R. Jackson, J.E. Moe, K.L. Williams, "Modeling of subcritical penetration into sediment due to interface roughness" in N.G. Pace E. Pouliquen, O. Bergem, and A.P. Lyons, editors, "High Frequency Acoustics in Shallow Water" SACLANTCEN CP-45, Lerici, July 1997.

[9] H.J. Simpson, B.H. Houston, " A synthestic array measurement of a fast compressional and a slower wave in an unconsolidated water-saturated porous medium", *Journal of the Acoustical Society of America* Vol. 102, No 5, Pt. 2, pp 3210, December 1997.

[10] D.R. Jackson, K.B. Briggs, K.L. Williams, and M.D. Richardson, "Tests of models for high-frequency seafloor scattering", *IEEE J. Ocean. Eng.* Vol 21 (4), 458-470, October 1996.

[11] Sleath, J.F.A. "Sea Bed Mechanics", Wiley, 1984.

[12] T. Akal and J. Hovem, "Two dimensional space series analysis for sea-floor roughness", *Marine Geotechnol.* Vol 3 (2), 171-182, 1978.

[13] K.B. Briggs, "Microtopographical roughness of shallow-water continental shelves", *IEEE J. Ocean. Eng.* Vol 14 (4), 360-367, October 1989.

[14] R.A. Wheatcroft, "Temporal variation in bed configuration and one-dimensional bottom roughness at the mid-shell STRESS site", *Continental Shelf Research* 14 (10/11), 1167-1190, 1994.

[15] K.B. Briggs, "High-frequency acoustic scattering from sediment interface roughness and volume inhomogeneities", Naval Research Laboratory, Stennis Space Center, MS, Tech. Rpt. No. NRL/FR/7431–94-9617, 1994.

[16] D.R. Jackson and K.B. Briggs, "High-frequency bottom backscattering: Roughness versus sediment volume scattering", *Journal of the Acoustical Society of America* 92 (2), 962-977, January 1988.

[17] M. F. Barnsley, R. L. Devaney, B. B. Mandelbrot, H. O. Peitgen, D. Saupe and R. F. Voss , "The science of fractal images", (Springer-Verlag 1988).

[18] C.S. Clay & H. Medwin, "Acoustical Oceanography: Principles and Applications", Wiley, New York, 1970, Chap. 10, Append. 10.

[19] E. Pouliquen, O. Bergem, G. Canepa, N.G. Pace "Time evolution Modeling of Seafloor Scatter, Part 1: Theory", SACLANTCEN M-328, La Spezia, Italy, 1997.

[20] R.J. Wagner, "Shadowing of randomly rough surfaces", *Journal of the Acoustical Society of America* 41, 138-147, 1967.

[21] L. Brekhovskikh, Y. Lysanov, "Fundamentals of Ocean Acoustics", Springer-Verlag, 1982.

[22] E.I. Thorsos, "The validity of the Kirchhoff approximation for rough surface scattering using a gaussian roughness spectrum", *Journal of the Acoustical Society of America* 83 (1), 78-92, January 1988.

[23] H. Schmidt, J. Lee, H. Fan, K. LePage, "Multistatic bottom reverberation in shallow water", in N.G. Pace E. Pouliquen, O. Bergem, and A.P. Lyons, editors, "High Frequency Acoustics in Shallow Water" SACLANTCEN CP-45, Lerici, July 1997.

Annex A

Validity of the Kirchhoff approximation

In the case of water-seafloor-water scattering, according to Brekhovskikh [21], for a deterministic surface, the following local criterion has to be satisfied in order that the Kirchhoff approximation may be used:

$$P = 2k_1 r_c(\mathbf{R}) \sin(\theta_g) \gg 1. \tag{32}$$

P will here be referred to as the Rayleigh parameter even though it is mostly known as having the following form: $P = 2k_1\sigma_s \sin(\theta_g)$ where σ_s corresponds to the surface rms roughness. Here, $k_1 \sin(\theta_g)$ is the normal component of the incident wavenumber and $r_c(\mathbf{R})$ is the local radius of curvature at point $\mathbf{R}$, θ_g is the local grazing angle of the incident sound wave. Before any further consideration, it is important to bear in mind that this condition has only been considered and tested for a water-seafloor-water scattering (in the case of monostatic and bistatic scattering in the same medium [22]). For a random rough surface, the Rayleigh parameter is expressed differently than in Eq. (32). The local radius of curvature $r_c(\mathbf{R})$ is replaced by the rms radius of curvature $\tilde{r}_c$:

$$P = 2k_1 \tilde{r}_c \sin(\theta_g) \gg 1. \tag{33}$$

Using the spectrum $W(\mathbf{K})$ of Eq. (1) and considering for simplicity the isotropic case (e.g. $K_c = 0$), $l_x = 0$ and $l_y = 0$, the rms slope s and rms radius of curvature $\tilde{r}_c$ take this analytical form:

$$s^2 = \sigma_s^2\{K_{hp}^2 + \frac{2}{l^2}\} \tag{34}$$

$$1/\tilde{r}_c^2 = \sigma_s^2(K_{hp}^4 + \frac{4}{l^2}\{K_{hp}^2 + \frac{2}{l^2}\}). \tag{35}$$

Figures 16 and 17 present the evolution of the Rayleigh parameter versus grazing angle at $f = 5$ kHz. The curves are parametrized by the correlation length l and by the rms height σ_s. At 5 kHz, in the 10° – 30° range, condition (33) is not satisfied for seafloors having a ratio σ_r/l larger than 0.15 (for example in the case of $\sigma_s = 4$

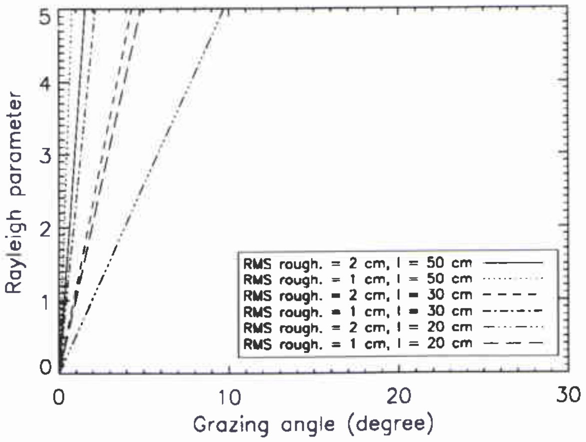

Figure 16 Rayleigh parameter for various roughnesses and correlation lengths. The roughness is isotropic ($K_c = 0$), the cut-off spatial wavenumber K_{hp} is set to 0 rad/m and the sound wave frequency is set to 5 kHz.

cm and l = 20 cm). This excludes rough seafloors (i. e. $\sigma_r > 3$ cm) having short correlation lengths ($l <$ 20 cm). For smoother seafloors with longer correlation length ($l \geq$ 20 cm), eq. (33) is satisfied above 15° providing that K_{hp} is not too large ($\leq$ 10 rad/m). Comparison between Figs. 16 and 17 shows that the greater is K_{hp}, the lower is P especially for seafloors with long correlation length. The value K_{hp} = 10 rad/m should be considered as a maximum value for sandy seafloors. The typical critical angle for sand is usually around 25 – 30°. Any model based on the Kirchhoff approximation intending to quantify the sub-critical penetration into sandy seafloors should not be used at grazing angles lower than 10° to 15° if the frequency is as low as 2-3 kHz. But above this limit, for smooth long-correlated surfaces, the Kirchhoff approximation seems to be a reasonable approximation.

For non isotropic seafloor, the validity of the Kirchhoff approximation is more difficult to evaluate. Firstly, the computation of the Rayleigh parameter cannot be made analytically and secondly, it depends on the orientation of the ripple field. On computer generated seafloor surfaces whose spectrum is non-centred gaussian, it is possible to obtain an approximate value of P. Figure 18 shows the computed evolution of P versus the grazing angle for 3 different orientations of the ripple field. Along the ripple field (e.g. skewness = 90°, which means that the incident sound wave is parallel to the crests of the ripple field), the rms radius of curvature is obviously larger than across the ripple field and in this case, the validity of the Kirchhoff approximation is easily obtained above 15° for rms height lower than 2 cm. However, across the ripple field and even for a skewness of 30°, the Rayleigh parameter is not much larger than unity above 15° grazing angle.

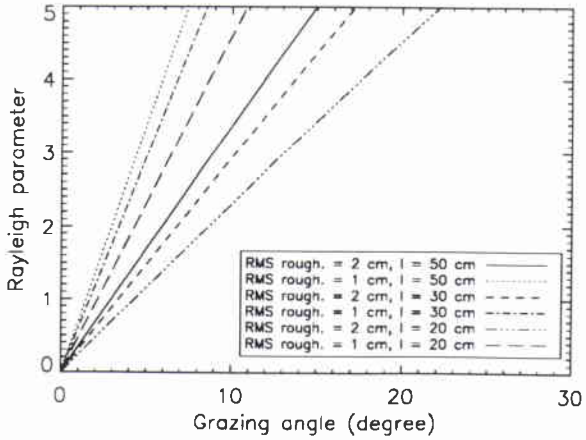

Figure 17 Rayleigh parameter for various roughnesses and correlation lengths. The roughness is isotropic ($K_c = 0$), the cut-off spatial wavenumber K_{hp} is set to 10 rad/m and the sound wave frequency is set to 5 kHz.

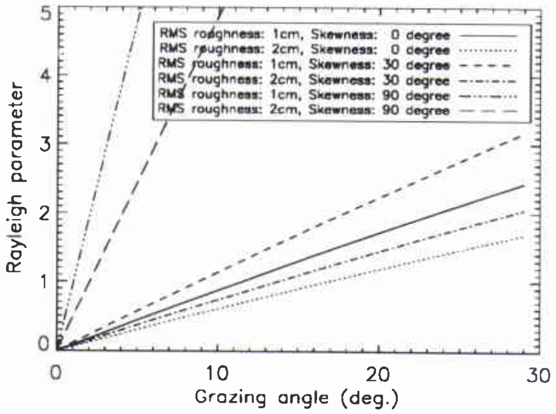

Figure 18 Rayleigh parameter computed from an artificial surface whose spectrum is a non centred gaussian ($K_c = 31$ rad/m which correspond to a 20 cm ripple field wavelength). The cut-off spatial wavenumber K_{hp} is set to 10 rad/m and the sound wave frequency is set to 5 kHz.

Annex B

Multiple reflection effects

Another limitation of the H-K integral is that it does not account for multiple scattering. This phenomenon is difficult to quantify and its effect on total penetration is also likely to increases at low grazing angles. Thorsos [22] noticed that multiple scattering had to be considered for grazing angles less than twice the rms slope s in the case of water-seafloor-water scattering. But no test has ever been made in order to evaluate the impact of multiple scattering on the resulting pressure field across the rough surface, within the sediment itself. This effect could be of a second order of magnitude as well as dominating at very low grazing angle. In our case (frequency as low as 2-3 kHz, rms roughness as high as 3 cm and correlation length as short as 20 cm), the condition of Thorsos is not fulfilled and multiple scattering should ideally be taken into account. Figure (19) shows the increase of the rms slope s as the rms roughness σ_s increases. For $\sigma_s > 1.2$ cm, it seems that multiple scattering is not of secondary importance for grazing angles smaller than 20° for values of K_{hp} up to 10 rad/m. However, at lower rms roughnesses (e.g. around 1 cm), multiple scattering effect may be ignored.

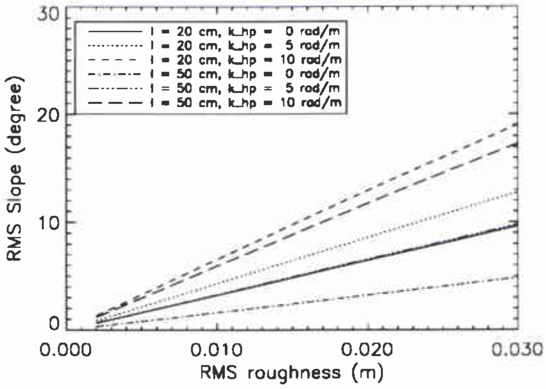

Figure 19 Evolution of the rms slope vs. the rms roughness for 2 different correlation lengths and 3 different cut-off spatial frequencies (0, 5 and 10 rad/m). In this case, $K_c = 0$

Annex C

Model-Data Comparison

Taken from Maguer [1], Figs. 20 and 21 present a comparison between data acquired at sea on a sandy seabed at Elba Island (Italy), the model presented in this report -referenced to as "Kirchhoff"- and a model developed by Schmidt [23]. This latter model combines a three dimensional version of OASES to compute the coherent field, and a wavenumber integration approach based on the perturbation approach to compute the scattering field. The acoustic data acquisition was performed simultaneously with a careful measurement of the environmental conditions. The geometry of acquisition was also controlled carefully, allowing a maximum uncertainty of the grazing angle of ±2° and of the burial depth of the hydrophones of ± 5 cm.

On each figure, two different grazing angles, one above critical and one below critical, are considered. The two models presented here produce a single realisation of the penetration ratio which of course cannot be similar to the penetration ratio computed by averaging a large number of received pings. However, agreement between data and models is good for all cases presented here (e.g. above and below critical, at 30 cm and 60 cm burial depth). The small discrepancies between data and model can be caused by the uncertainties mentioned above, as well as the difficulties in approximating the directivity pattern of the parametric source used in this experiment. However, the relative good agreement between data and models tends to strengthen the approach presented in this report and the pertinence of using the Kirchhoff approximation in this frequency and angular range.

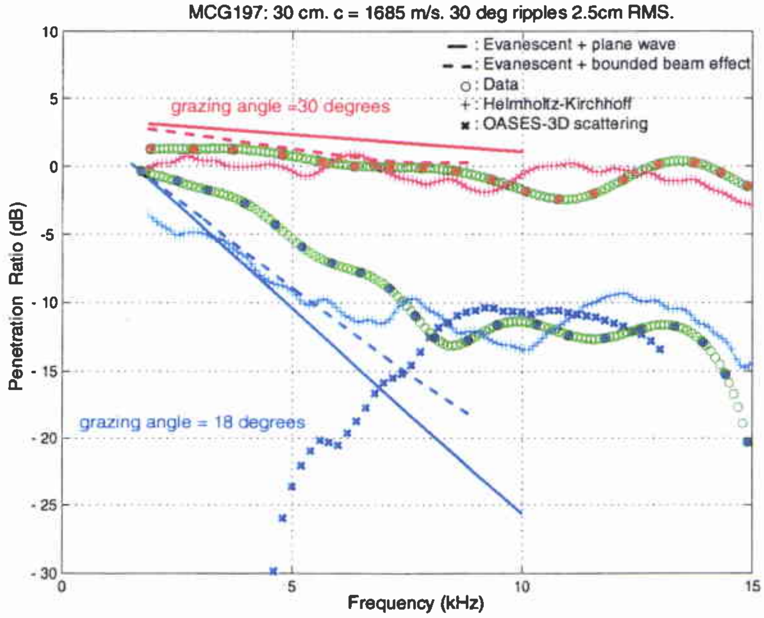

Figure 20 Measured and modeled penetration ratio for hydrophone located 30 cm below the interface

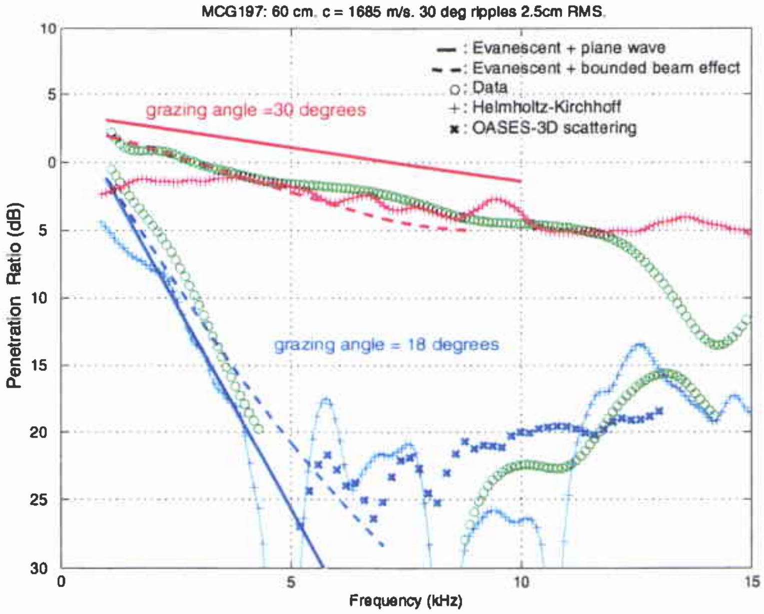

Figure 21 Measured and modeled penetration ratio for hydrophone located 60 cm below the interface

Report no. changed (Mar 2006): SR-290-UU

Document Data Sheet

Security Classification		*Project No.* 033-2
Document Serial No. SR-290	*Date of Issue* August 1998	*Total Pages* 43 pp.

Author(s)

Pouliquen, E., Lyons, A.P., Pace, N.G.

Title

Penetration of acoustic waves into sandy seafloors at low grazing angles: the Helmholtz-Kirchhoff approach.

Abstract

The Helmholtz-Kirchhoff integral is applied to model the penetration of sound waves into sandy seafloors at grazing angles above and below the critical angle. Although the conditions for the validity of the Kirchhoff approximation can be limiting, this approximation should be valid at high frequency for gently undulating seafloor surfaces even at moderate to low grazing angles, providing that the self-shadowing effect is carefully removed. The analytical development of the method is first presented, followed by numerical examples. Simulations and data acquired at sea are in very good agreement in the 2-15 kHz band (Maguer *et al.*} [SACLANTCEN Report, SR-287, April 1998]). The model predicts, in agreement with the 2-15 kHz acoustic data, the frequency at which the contributions due to roughness effects begin to dominate those due to the evanescent wave. Secondary effects such as Bragg interference patterns and the loss of signal coherence with grazing angle or depth are correctly predicted. The model simulations strongly suggest that roughness of the sediment interface is most likely the cause of anomalous sound penetration into the seabed.
Résumé:}

Keywords

seafloor– surface scattering –sound penetration –Kirchhoff– evanescent wave – time domain

Issuing Organization

North Atlantic Treaty Organization
SACLANT Undersea Research Centre
Viale San Bartolomeo 400, 19138 La Spezia, Italy

[From N. America: SACLANTCEN
(New York) APO AE 09613]

Tel: +39 0187 527 361
Fax:+39 0187 524 600

E-mail: library@saclantc.nato.int

Report no. changed (Mar 2006): SR-290-UU

Initial Distribution for SR 290

Ministries of Defence

DND Canada		10
CHOD Denmark		8
DGA France		8
MOD Germany		15
HNDGS Greece		12
MARISTAT Italy		9
MOD (Navy) Netherlands		12
NDRE Norway		10
MOD Portugal		5
MDN Spain		2
TDKK and DNHO Turkey		5
MOD UK		20
ONR USA	32 if classified	34

NATO Commands and Agencies

NAMILCOM	2
SACLANT	3
CINCEASTLANT/ COMNAVNORTHWEST	1
CINCIBERLANT	1
CINCWESTLANT	1
COMASWSTRIKFOR	1
COMMAIREASTLANT	1
COMSTRIKFLTANT	1
COMSUBACLANT	1
SACLANTREPEUR	1
SACEUR	2
CINCNORTHWEST	1
CINCSOUTH	1
COMEDCENT	1
COMMARAIRMED	1
COMNAVSOUTH	1
COMSTRIKFORSOUTH	1
COMSUBMED	1
NC3A	1
PAT	1

Scientific Committee of National Representatives

SCNR Belgium	1
SCNR Canada	1
SCNR Denmark	1
SCNR Germany	1
SCNR Greece	1
SCNR Italy	1
SCNR Netherlands	2
SCNR Norway	1
SCNR Portugal	1
SCNR Spain	1
SCNR Turkey	1
SCNR UK	1
SCNR USA	2
French Delegate	1
SECGEN Rep. SCNR	1
NAMILCOM Rep. SCNR	1

National Liaison Officers

NLO Canada	1
NLO Denmark	1
NLO Germany	1
NLO Italy	1
NLO Netherlands	1
NLO Spain	1
NLO UK	1
NLO USA	1

198 if classified	**Sub-total**	200
	SACLANTCEN	30
228 if classified	**Total**	230